

pubs.acs.org/cm Article

Combined Experimental and Theoretical Investigations of n-Type BiFeO₃ for Use as a Photoanode in a Photoelectrochemical Cell

Andjela Radmilovic, Tyler J. Smart, Yuan Ping, and Kyoung-Shin Choi*



Cite This: Chem. Mater. 2020, 32, 3262-3270



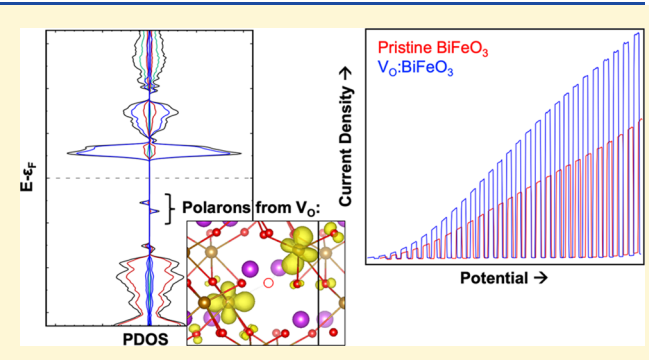
ACCESS

Metrics & More

Article Recommendations

Supporting Information

ABSTRACT: Combined experimental and theoretical investigations were performed to evaluate the potential of n-type BiFeO $_3$ as a photoanode. While previous experimental and theoretical studies on BiFeO $_3$ mainly focused on its ferroelectric properties, several studies have reported the advantages of BiFeO $_3$ as a photoelectrode for solar water splitting (e.g., bandgap energy and band-edge positions relative to water reduction and oxidation potentials). However, the photoelectrochemical properties of n-type BiFeO $_3$ have not yet been thoroughly investigated. In our experimental investigation, we developed an electrodeposition-based synthesis to prepare uniform n-type BiFeO $_3$ thin-film electrodes. Furthermore, using a heat treatment under a N_2 environment, we intentionally introduced



additional oxygen vacancies into the pristine n-type BiFeO₃ electrodes to increase the majority carrier density. The bandgaps, flatband potentials, photocurrent onset potentials, photocurrent generation, and photoelectrochemical stabilities of the pristine and N₂-treated BiFeO₃ photoanodes were investigated comparatively to improve our understanding of BiFeO₃ photoanodes and to examine the effect of oxygen vacancies on the photoelectrochemical properties of BiFeO₃. In our theoretical investigation, we performed first-principles calculations and demonstrated the formation of a small polaron when an extra electron was introduced into the BiFeO₃ lattice. Changes in electronic states caused by the small polaron formation were carefully investigated. We also examined the effects of oxygen vacancies on electron-polaron formation and carrier concentration in BiFeO₃. Using charge formation energy calculations and referencing charge transition levels to the free electron-polaron level instead of to the conduction band minimum, we showed that the oxygen vacancy is capable of serving as a donor to enhance the carrier concentration of BiFeO₃. Our theoretical results agree well with our experimental findings. Together, the new experimental and theoretical results and discussion provided in this study have considerably improved our understanding of n-type BiFeO₃ as a photoanode.

1. INTRODUCTION

Bismuth iron oxide, BiFeO₃, is a semiconductor with a rhombohedrally distorted perovskite structure that yields a large ferroelectric effect. For this reason, it has been investigated as one of the most promising candidates for ferroelectric diode devices and ferroelectric photovoltaics. 1-4 Recently, BiFeO₃ was also reported as a photoelectrode in a solar water-splitting cell. 5-9 In these reports, BiFeO₃ was demonstrated to have a relatively narrow bandgap of ~2.2 eV and conduction band minimum (CBM) and valence band maximum (VBM) positions that straddle the water reduction and oxidation potentials, 5,6 all of which are very attractive features for a photoelectrode in a water-splitting photoelectrochemical cell (PEC). Considering that Fe₂O₃, an extensively studied photoanode with a similar bandgap, has a CBM that is ~200 mV more positive than the water reduction potential, 10 the shifts in the CBM and VBM to the negative direction constitute an important advantage of BiFeO3 over Fe_2O_3 .

To date, both n-type and p-type BiFeO₃ photoelectrodes have been reported, 5-9 meaning that BiFeO₃ can serve as a

photoanode and a photocathode, respectively. In these studies, the doping type varied without the introduction of external dopants, suggesting that the defects responsible for n-type and p-type BiFeO₃ can both readily form. The defects that cause n-type behavior include oxygen vacancies, and the defects that cause p-type behavior include Bi vacancies.

Despite the many interesting and advantageous features shown for BiFeO₃ as a photoelectrode, there have been very few systematic investigations on the photoelectrochemical properties of BiFeO₃. Because of its popularity as a ferroelectric material, most studies on BiFeO₃ photoelectrodes have focused on how the application of an external electric field on BiFeO₃ affects its photocurrent generation or on the

Received: February 8, 2020 Revised: March 13, 2020 Published: April 2, 2020





conversion between n-type and p-type photocurrent. Ry,9,14,15 From a careful analysis of these papers, it appears that the BiFeO $_3$ electrodes used in these studies were very lightly doped. For the purpose of accurately evaluating the potential of BiFeO $_3$ as a photoanode or a photocathode, optimally doped n-type and p-type BiFeO $_3$ electrodes need to be prepared and examined individually.

Considering that charge transport in many oxide-based photoanodes involves small polaron hopping, ^{16–21} understanding the formation and transport of small polarons in BiFeO₃ is also critical. Unfortunately, while numerous theoretical studies on BiFeO₃ have been published to date, they have focused on its bulk polarization, ^{22,23} photovoltaic effects, ^{24,25} and multiferroic effects. ^{26,27} Small electron-polaron formation and its effects on dopant ionization energies and concentration of free carriers in BiFeO₃ have not yet been investigated theoretically.

In this work, we conducted combined experimental and theoretical studies on n-type BiFeO₃ photoanodes. For the experimental investigation, we prepared highly uniform BiFeO₃ photoanodes by electrodeposition and examined their photoelectrochemical properties and stability for use in a PEC. We then intentionally introduced oxygen vacancies into the pristine BiFeO₃ lattice and examined the effect on carrier concentration and photocurrent generation. The experimental results were compared with those of a computational study, which examined the formation of small polarons in BiFeO₃ and the effect of oxygen vacancies on small polaron formation and free carrier generation in BiFeO₃ for the first time. The new experimental and computational results discussed in this study will significantly increase our fundamental understanding of BiFeO₃ for use as a photoanode material.

2. EXPERIMENTAL SECTION

Experimental Methods. *Materials.* Bismuth(III) nitrate (Bi-(NO₃)₃·5H₂O, 98%) and sodium sulfite (Na₂SO₃, 98%) were purchased from Sigma-Aldrich. Iron(II) chloride (FeCl₂·4H₂O, 98%) and potassium perchlorate (KClO₄, 99–100.5%) were purchased from Alfa-Aesar. Dimethyl sulfoxide (DMSO, 99.9%) was purchased from VWR Chemicals. All chemicals were used as purchased without further purification. Glass substrates coated with fluorine-doped tin oxide (FTO) were purchased from Hartford Glass Co. and cleaned thoroughly prior to use.

Preparation of BiFeO₃ Electrodes. Coelectrodeposition of Bi and Fe metals in a 1:1 ratio was carried out in an undivided cell using a VSP multichannel potentiostat (BioLogic). A typical 3-electrode setup with an FTO working electrode, a Ag/AgCl (4 M KCl) reference electrode, and a Pt counter electrode was used. The Pt CE was prepared by sputter coating 20 nm of titanium followed by 100 nm of platinum onto a clean glass slide.) The exposed area of the FTO working electrode was ~1.2 cm². The plating solution prepared here contained 14 mM Bi(NO₃)₃·5H₂O₂ 21 mM FeCl₂·4H₂O₂ and 100 mM KClO₄ in DMSO, which was purged with N₂ for 10 min before addition of precursors. KClO₄ was used as a supporting electrolyte. The entire solution was purged with N₂ for 30 s prior to the deposition to remove any remaining oxygen from solution and to prevent oxidation of the iron precursor. A potentiostatic deposition was used with an applied potential of -1.8 V vs Ag/AgCl and a total charge passed of 100 mC/cm². The time required to deposit a single film was <1 min. Immediately after deposition, the films were washed with ethanol and blow-dried with air. The films were black in color. The Bi:Fe ratio was determined to be 1:1 using energy-dispersive Xray spectroscopy (EDS).

To convert the BiFe films to BiFeO $_3$, the as-deposited films were annealed in air at 600 °C for 3 h (ramp rate 6.7 °C/min). The resulting films were orange in color.

 N_2 treatment was carried out by annealing pristine BiFeO $_3$ under N_2 gas (flow rate 75 cc/min) at 500 °C for 2 h (2 h purge, ramp rate 4.2 °C/min).

Materials Characterization. The purity and crystallinity of the BiFeO₃ electrodes were characterized by X-ray diffraction (XRD; D8 Discover, Bruker, Ni-filtered Cu K α radiation, $\lambda = 1.5418$ Å). The surface morphology and elemental composition were determined by scanning electron microscopy (SEM; Leo Supra55 VP, accelerating voltage 2 kV) and energy-dispersive X-ray spectroscopy (EDS; Noran System Seven, Thermo-Fisher, ultradry silicon drift detector, accelerating voltage 22 kV), respectively. Bandgaps were determined from UV-visible (UV-vis) absorption spectra obtained using an integration sphere to collect all reflected and transmitted light, allowing for more accurate determination of absorbance (Cary 5000 UV-vis-NIR spectrophotometer, Agilent). X-ray photoelectron spectroscopy (XPS) spectra were measured using a K-Alpha X-ray photoelectron spectrometer (Thermo Fisher Scientific) equipped with monochromatic Al K α excitation (1486.6 eV). The binding energies were calibrated with respect to the adventitious carbon 1s peak at 284.5 eV.

Photoelectrochemical and Electrochemical Characterization. All photoelectrochemical and electrochemical measurements were conducted with an SP-200 potentiostat/EIS (Bio-Logic Science Instrument). Solar illumination was simulated by filtering light from a 300 W Xe arc lamp through the following successive filters: water IR filter, neutral density filters, and an AM 1.5 G filter. The light was collimated and directed onto the sample via an optical fiber, and the light was calibrated to 100 mW/cm² (1 sun) using an NREL-certified GaAs reference cell (PV Measurements). The working electrode was masked with lacquer to ensure that the exposed geometric area of the electrode (~0.02 cm²) was smaller than the illuminated area (0.06 cm²). The electrode was illuminated through the glass side first (back-side illumination). A typical 3-electrode setup was used in an undivided cell with a BiFeO₃ working electrode, a Ag/AgCl (4 M KCl) reference electrode, and a Pt counter electrode.

To probe the n-type behavior of BiFeO₃, J-V plots were obtained under chopped illumination by sweeping the potential to the positive (oxidative) direction with a scan rate of 10 mV/s. Measurements for sulfite oxidation were conducted in a buffered solution containing 0.25 M H₃BO₃ and 0.7 M Na₂SO₃ (pH 9.2, adjusted with KOH). Measurements for water oxidation were carried out in a solution containing only 0.25 M H₃BO₃ (pH 9.2, adjusted with KOH). These solutions will be referred to as "pH 9.2 borate buffer" throughout the paper, and the species being oxidized will be specified (i.e., sulfite or water). J-t plots were measured at a constant potential of 0.8 V vs RHE for sulfite oxidation in pH 9.2 borate buffer.

All results in this work are presented with respect to the reversible hydrogen electrode (RHE) for easy comparison with reports using various pH conditions. Potentials vs Ag/AgCl were converted to potentials vs RHE as follows

$$E \text{ (vs RHE)} = E \text{ (vs Ag/AgCl)} + E_{Ag/AgCl} + 0.0591 \text{ V} \times \text{pH}$$

where $E_{\rm Ag/AgCl}$ (reference electrode, 4 M KCl) = 0.1976 V vs NHE at 25 °C.

Mott–Schottky measurements were obtained in the dark using a typical 3-electrode setup composed of a BiFeO₃ working electrode masked with electroplating tape 370 (3M, 0.12 cm² exposed area), a Ag/AgCl (4 M KCl) reference electrode, and a Pt counter electrode in the same sulfite-containing solution used for photoelectrochemical measurements (pH 9.2 borate buffer). A sinusoidal modulation of 10 mV was applied at frequencies of 0.5, 2, and 5 kHz.

Computational Methods. Density functional theory calculations were performed using the Quantum ESPRESSO package²⁸ with PBE +U exchange-correlation functional, ultrasoft pseudopotentials,²⁹ and Hubbard U parameters of 2 eV on O 2p and 3 eV on Fe 3d. All calculations were done using the hexagonal BiFeO₃ cell (space group R3c), which we expanded to a $2 \times 2 \times 1$ supercell to avoid spurious interactions during defect calculations. A $2 \times 2 \times 2$ k-point grid was used to calculate the charge density, and a $4 \times 4 \times 4$ k-point grid was

used for density of states. We applied a newly developed charge correction scheme 30 to calculations containing excess charge as implemented in JDFTx. 31

For the calculations used to investigate the effect of oxygen vacancies, a single oxygen atom was removed from a 120-atom supercell. Because 72 oxygen atoms are present in this supercell, this is equivalent to removing 1.39 atom % oxygen (1.39 oxygen atoms out of 100 oxygen atoms), leading to the empirical formula of BiFeO_{2.96}.

Theoretical optical absorption spectra of BiFeO₃ with and without an oxygen vacancy were obtained by computing the imaginary part of the dielectric function in the random phase approximation with local field effects as implemented in the YAMBO code. The input of this calculation came directly from our single-particle eigenvalues and wave functions from DFT+U computed in Quantum ESPRESSO. The absorption spectrum (α) is related to the real and imaginary parts of the dielectric function (ϵ_1 and ϵ_2 , respectively) as shown in the equation 33

$$\alpha(\omega) = \frac{\omega}{c} \frac{\epsilon_2(\omega)}{\sqrt{\frac{\epsilon_1(\omega) + \sqrt{\epsilon_1(\omega)^2 + \epsilon_2(\omega)^2}}{2}}}$$

3. RESULTS AND DISCUSSION

Experimental Study. The BiFeO₃ electrodes investigated in this study were prepared via coelectrodeposition of Bi and Fe metals followed by annealing in air. For the coelectrodeposition, the precursor concentrations in the plating solution were carefully optimized to produce films with a 1:1 ratio of Bi:Fe as confirmed by energy-dispersive X-ray spectroscopy (EDS). Because the reduction potential of Bi³⁺ is more positive than that of Fe²⁺, it can be reduced more easily, meaning that a lower concentration of Bi³⁺ relative to Fe²⁺ was necessary to achieve the desired ratio of Bi:Fe in the deposited films. The X-ray diffraction (XRD) pattern of the as-deposited films shown in Figure 1 contained a Bi peak but no Fe peaks, indicating that

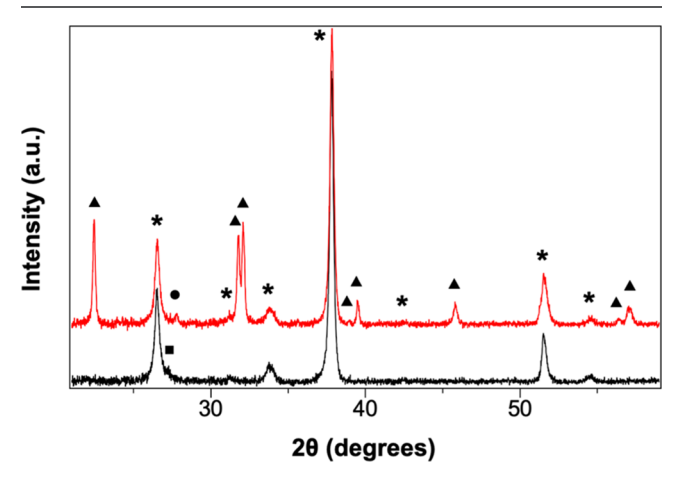


Figure 1. XRD patterns of as-deposited BiFe film (black) and annealed BiFeO₃ film (red). Asterisks (*) indicate peaks from the FTO substrate, square (■) indicates Bi metal, and triangles (\blacktriangle) indicate BiFeO₃ peaks (space group R3c; PDF No. 66-0439). Bi₂O₃ impurity peak is marked with a circle (\blacksquare).

the as-deposited film is composed of a mixture of crystalline Bi and amorphous Fe metals. The peak position for Bi matches well with the main peak expected for pure Bi metal, suggesting that no alloys of Bi and Fe were formed.³⁴

The as-deposited film was converted to crystalline BiFeO₃ upon annealing in air at 600 °C. The XRD pattern of the annealed film confirmed the formation of crystalline BiFeO₃. A

very small peak corresponding to Bi_2O_3 was observed in the XRD pattern at $2\theta \approx 27.5^{\circ}$. Judging from the peak intensity, however, the amount was negligible, and Bi_2O_3 is not expected to interfere with the evaluation of the photoelectrochemical properties of $BiFeO_3$ due to its large bandgap. We note that the average surface atomic ratio of Bi:Fe for the $BiFeO_3$ electrode obtained by X-ray photoelectron spectroscopy (XPS) was 1.04:1, indicating that there was no obvious surface enrichment of either Bi or Fe (Figure S1).

Scanning electron microscopy (SEM) images of the asdeposited films are shown in Figure 2a and reveal a uniform,

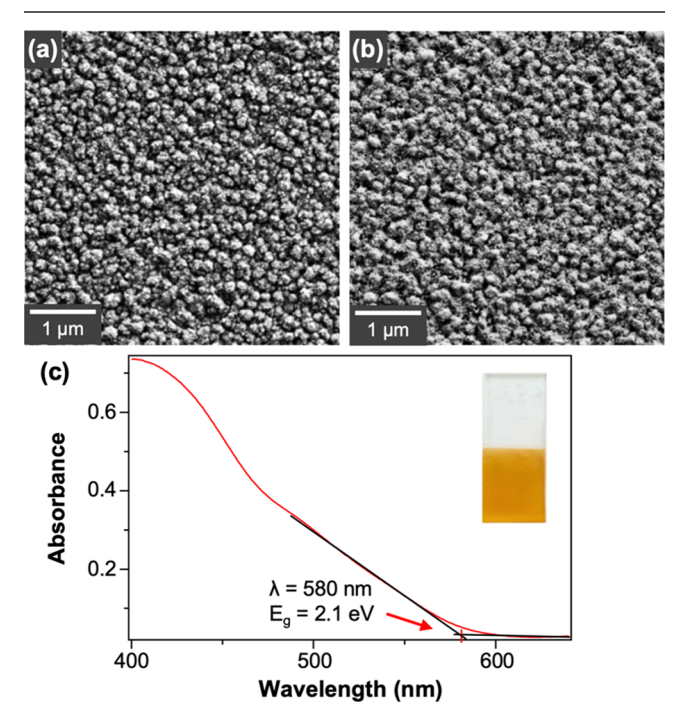
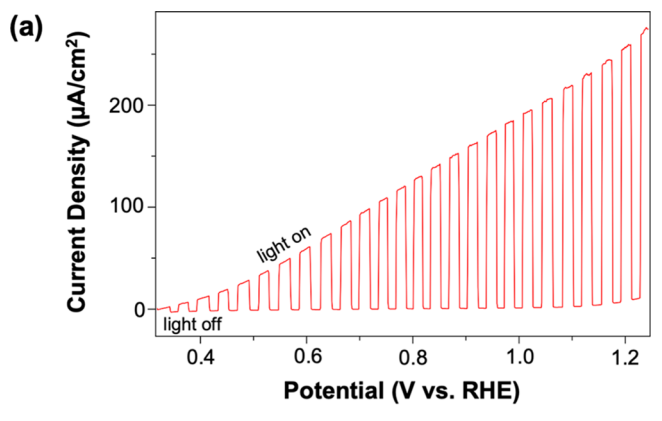


Figure 2. SEM images of (a) as-deposited BiFe film and (b) annealed (pristine) BiFeO₃ film. (c) UV–vis spectrum for BiFeO₃, where the inset shows a photograph of the pristine film.

compact morphology with very small grain size and full substrate coverage. Upon annealing, the morphology remained very similar (Figure 2b). A film thickness of \sim 120 nm was determined by cross-sectional SEM (Figure S2). (The film thickness was optimized for the highest photocurrent generation.) The UV–visible (UV–vis) absorption spectrum in Figure 2c shows an absorption onset of \sim 580 nm, corresponding to a bandgap energy of 2.1 eV, which agrees with the visible orange color of the film as seen in the inset of Figure 2c.

The photoelectrochemical performance of BiFeO₃ was first investigated using sulfite oxidation. Sulfite is an effective hole scavenger whose oxidation kinetics are significantly faster than those of water oxidation. Therefore, measuring the photocurrent for sulfite oxidation allows us to evaluate the ability of a photoanode to generate photocurrent without the limitation of slow interfacial kinetics for water oxidation.³⁵ In other words, the photocurrent generated by a BiFeO₃ photoanode for sulfite oxidation can be considered to be the maximum photocurrent that a BiFeO₃ photoanode can generate for water oxidation when paired with an appropriate oxygen evolution catalyst.

Figure 3a shows the J-V plot of pristine BiFeO₃ for sulfite oxidation obtained under illumination equivalent to 1 sun (100



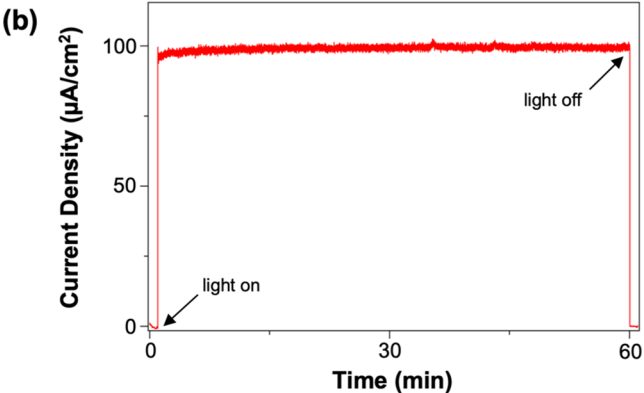


Figure 3. (a) J-V plots and (b) J-t plots at 0.8 V vs RHE for pristine BiFeO₃ for sulfite oxidation. All measurements were obtained in pH 9.2 borate buffer containing 0.7 M sulfite under 1 sun illumination (100 mW/cm², AM 1.5 G).

mW/cm², AM 1.5G). Chopped illumination was used to compare the dark current and photocurrent in a single scan while simultaneously assessing the presence of transient photocurrent. As evidenced by the positive (oxidative) photocurrent, the BiFeO₃ electrodes were n-type as prepared, and the lack of transient photocurrent even in the potential region near the photocurrent onset indicates efficient use of surface-reaching holes for sulfite oxidation. The photocurrent density generated at 1.2 V vs RHE was ~250 μ A/cm², which, to the best of our knowledge, is the highest photocurrent generated by n-type BiFeO₃ as a single-component photoanode.

It is important to note that the photocurrent onset at ~ 0.3 V vs RHE is significantly more negative than that of other ternary Fe-based oxide photoanodes (e.g., ZnFe₂O₄, MgFe₂O₄, CuFe₂O₄). This negative photocurrent onset, which allows BiFeO₃ to achieve a high photovoltage for water oxidation, appears to be a distinctive advantage of BiFeO₃ over other Fe³⁺-containing photoanodes. The J-t plot in Figure 3b shows that the BiFeO₃ photoanode can generate stable photocurrent for sulfite oxidation in pH 9.2 borate buffer.

To investigate whether the introduction of more oxygen vacancies could enhance the n-type behavior of the BiFeO $_3$ photoanodes, the pristine BiFeO $_3$ electrodes were additionally annealed under nitrogen gas at 500 °C for 2 h. Compared with annealing under hydrogen gas, annealing under N $_2$ provides a milder reducing environment for generating oxygen vacancies. As a result, higher annealing temperatures and a longer annealing time are typically required when using a N $_2$ environment to create oxygen vacancies compared with a H $_2$

environment. However, because annealing under H_2 gas can induce hydrogen incorporation in addition to oxygen vacancies, 36,37 annealing under N_2 should introduce fewer variables into the samples, thus allowing for the unambiguous investigation of the effect of only oxygen vacancies. There have been a few cases in which annealing under nitrogen gas resulted in the incorporation of nitrogen into the compounds of interest, but these cases are very rare and have been limited to high-surface-area oxides containing vanadium ions that appear to have high nitrogen affinity.

The N_2 -treated BiFeO $_3$ showed no changes in absorbance, morphology, or XRD pattern in comparison with the pristine BiFeO $_3$ (Figures S3 and S4). In addition, X-ray photoelectron spectroscopy (XPS) was used to confirm that no nitrogen was incorporated into the films during N_2 treatment (Figure S1). Mott—Schottky plots did show a difference before and after the N_2 treatment, however, as seen in Figure 4. The slope of the

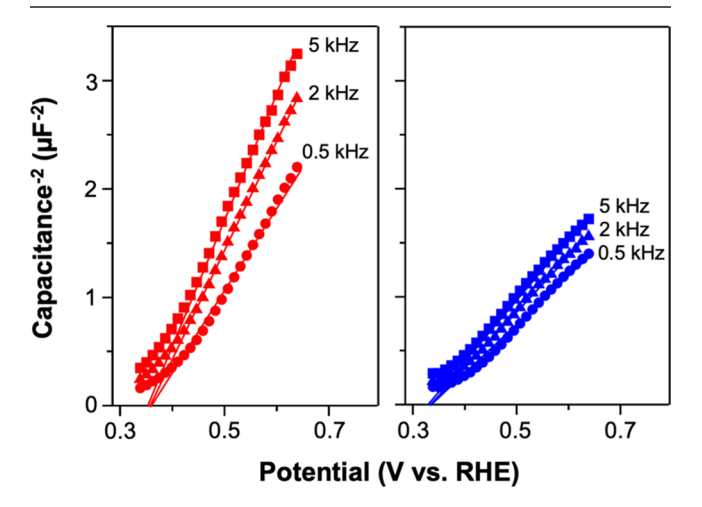
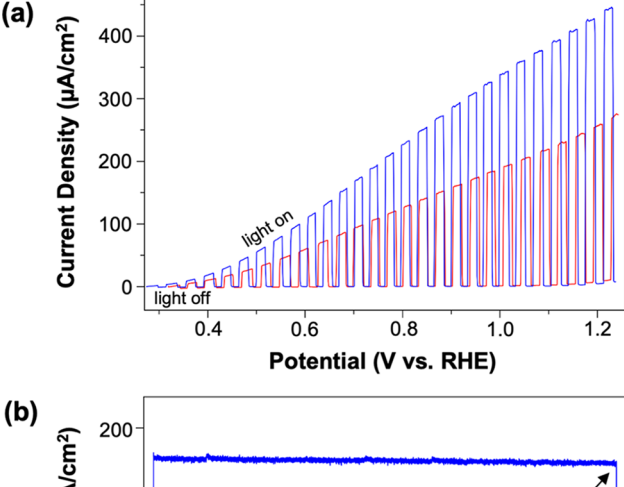


Figure 4. Mott–Schottky plots for pristine (red, left) and N_2 -treated (blue, right) BiFeO₃ at 0.5 (●), 2 (▲), and 5 kHz (■) frequencies. All measurements were obtained in pH 9.2 borate buffer containing 0.7 M sulfite.

linear region decreased noticeably in the plot for N_2 -treated BiFeO₃ relative to pristine BiFeO₃, signifying an increase in majority carrier density. This implies that the N_2 treatment indeed generated more oxygen vacancies, which function to increase the majority carrier density of BiFeO₃. To the best of our knowledge, this is the first report of intentionally enhancing the anodic photocurrent generation of BiFeO₃ by increasing the carrier density.

From the Mott–Schottky plots, the flatband potential ($E_{\rm FB}$) for pristine BiFeO $_3$ was estimated to be \sim 0.36 V vs RHE. The N $_2$ -treated sample showed a shift in the $E_{\rm FB}$ to the negative direction by \sim 20 mV, which agrees well with the increase in the carrier density. As the precise surface area of the BiFeO $_3$ electrodes was not known, their carrier concentrations could not be accurately determined. However, assuming a roughness factor of 2 and a dielectric constant of 53 for the BiFeO $_3$ electrodes, and a dielectric constant of pristine and N $_2$ -treated BiFeO $_3$ were approximated to be \sim 4.2 \times 10 18 and \sim 8.3 \times 10 18 cm $^{-3}$, respectively.

J-V plots for sulfite oxidation comparing the pristine and N_2 -treated BiFeO₃ photoanodes are shown in Figure 5a. The photocurrent generated by N_2 -treated BiFeO₃ was significantly higher than that generated by the pristine sample. Specifically,



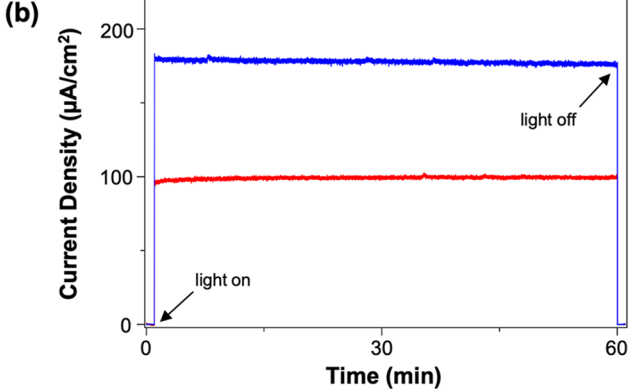


Figure 5. (a) J-V plots and (b) J-t plots at 0.8 V vs RHE for pristine BiFeO₃ (red) and N₂-treated BiFeO₃ (blue) for sulfite oxidation. All measurements were obtained in pH 9.2 borate buffer containing 0.7 M sulfite under 1 sun illumination (100 mW/cm², AM 1.5 G).

the photocurrent density at 1.2 V vs RHE increased from ~ 250 to $\sim 440 \ \mu\text{A/cm}^2$ upon N_2 treatment, corresponding to a 76% increase. Because the N_2 treatment did not enhance the photon absorption of BiFeO₃, the photocurrent enhancement observed for the N_2 -treated BiFeO₃ could be attributed solely to the additional oxygen vacancies formed, which increased the carrier density. The J-t plot in Figure 5b shows that the N_2 -treated sample is also stable for sulfite oxidation in pH 9.2 borate buffer.

We note that the N_2 -treated BiFeO₃ showed a photocurrent onset shifted to the negative direction by ~50 mV. Considering that the photocurrent onset potential measured using a hole scavenger with fast oxidation kinetics is one way to determine the $E_{\rm FB}$ of a photoanode, 35 it can be said that the $E_{\rm FB}$ values obtained from the Mott–Schottky and J-V plots agree well with each other. While the N_2 treatment considerably increased the photocurrent of our BiFeO₃ photoanodes, the resulting photocurrent was still far below that expected for a photoanode with a bandgap of 2.1 eV. This shows that bulk electron–hole recombination is a major limitation of BiFeO₃, and as with other Fe³⁺-containing photoanodes, nanostructuring will be required to alleviate bulk recombination and further enhance photocurrent. 40,41

J-V plots of pristine and N_2 -treated BiFeO $_3$ for water oxidation in pH 9.2 borate buffer is shown in Figure S5. The photocurrent generated for water oxidation was considerably lower (<5 μ A/cm 2 at 1.2 V vs RHE) than that generated for sulfite oxidation by both types of films, indicating that the surface of the BiFeO $_3$ prepared in this study is not catalytic for water oxidation and will need to be paired with an appropriate oxygen evolution catalyst when used in a photoelectrochemical water splitting cell.

Computational Study. To gain additional insight into the photoelectrochemical properties of BiFeO₃, we conducted density functional theory (DFT) calculations to investigate the small polaron formation and its effect on defect ionization energy and free carrier concentration in BiFeO₃. First-principles calculations were carried out on BiFeO₃ using the DFT+U method (see Computational Methods for more information). The computed bandgap of BiFeO₃ was 2.2 eV, which is in great agreement with the experimentally measured value of the bandgap.

Due to strong electron—phonon interactions, carriers in many transition metal oxides are trapped by their self-induced lattice distortions, forming small polarons. Small polarons conduct through the system via a thermally activated hopping mechanism unlike carriers in covalent semiconductors, which conduct through conventional band mechanisms. Therefore, understanding and facilitating small polaron hopping are critical for the development of oxide-based photoelectrodes. 16–18,20,45,46

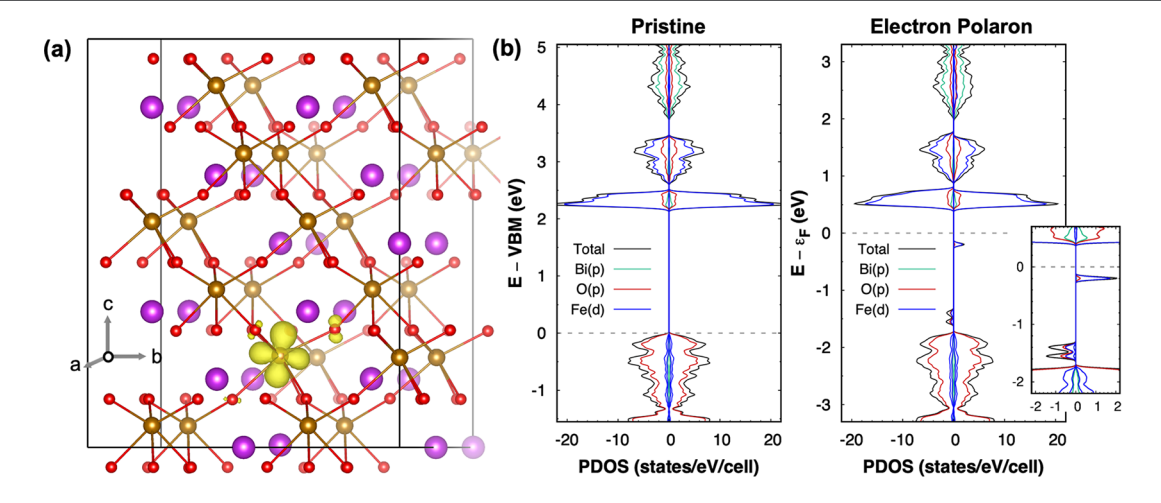


Figure 6. (a) Norm-squared wave function of the electron-polaron (yellow cloud) shown as an isosurface in the BiFeO₃ lattice (purple = Bi, gold = Fe, red = O). Isosurface value is 1% of the maximum amplitude of the wave function. (b) Projected density of states (PDOS) for BiFeO₃ before (left) and after (right) a single electron-polaron is introduced in a 120-atom supercell.

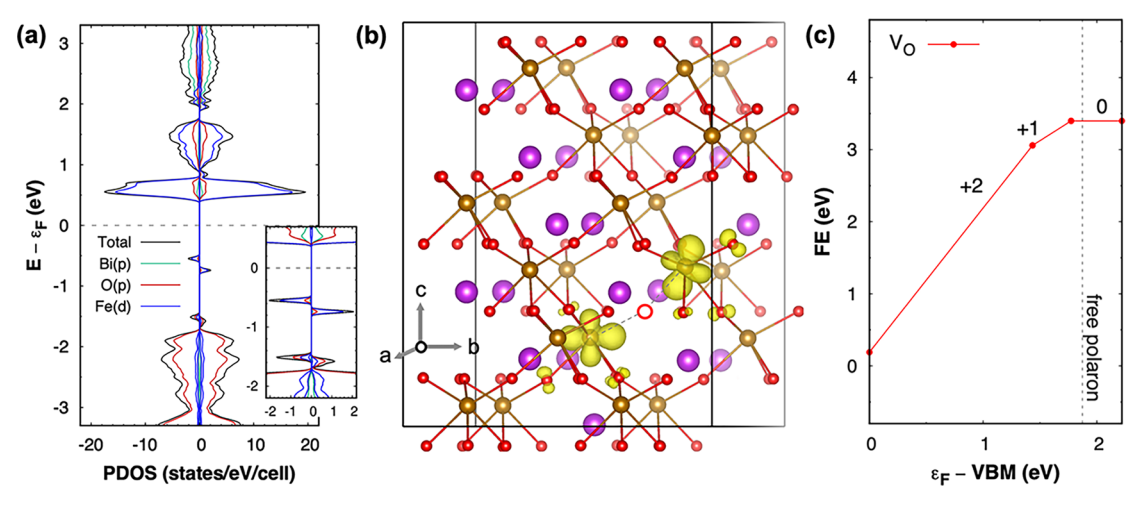


Figure 7. (a) Projected density of states (PDOS) for BiFeO₃ with a single oxygen vacancy (V_O) introduced into a 120-atom supercell. (b) Normsquared wave function of the two electron—polarons (yellow regions surrounding Fe). Isosurface value is 1% of the maximum amplitude of the wave function. V_O is indicated by a single empty red circle between the two electron—polarons. (c) Defect formation energy (FE) diagram of V_O in BiFeO₃.

Small Polaron Formation. Formation of an electron-polaron in pristine $BiFeO_3$ was simulated by adding one extra electron into the pristine $BiFeO_3$ system and allowing the system to relax. We observed that the extra electron spontaneously localizes on a single Fe site, forming a small electron-polaron as shown in Figure 6a. This creates a deep, localized state that lies 1 eV below the CBM of the pristine $BiFeO_3$ as shown in Figure 6b. Formation of similar localized electron-polaron states has been observed in other Fe^{3+} -based oxides such as Fe_2O_3 . 19

The Fe³⁺ ions in BiFeO₃ have O_h crystal field splitting with 3d⁵ high-spin electron configuration. Thus, the extra electron occupies an Fe t_{2g} state, and the small polaron state has mainly t_{2g} character. Furthermore, the presence of a small polaron on the Fe ion, which lowers its valency from +3 to +2, perturbs valence states and creates additional localized states above the VBM of the pristine BiFeO₃ (Figure 6b). These localized states have the character of e_g orbitals of Fe²⁺ and 2p orbitals of oxygen. (The corresponding wave functions are shown in Figure S6.)

Electronic Structure of V_O in BiFeO₃. Previous theoretical studies on defect formation in BiFeO₃ reported that the oxygen vacancy is a very deep donor with an ionization energy greater than 1 eV, 12,40,48,49 meaning that the oxygen vacancy cannot contribute to the generation of n-type carriers at room temperature. This disagrees with our experimental observation that the N2-treated BiFeO3 that contains more oxygen vacancies has a higher carrier density and generates significantly more photocurrent at room temperature. We note that previous theoretical studies did not consider the formation of small polarons in BiFeO₃ and their effects on defect ionization energies and carrier concentration. Employing recently developed methods, 19,20 we revisited the formation of oxygen vacancies in BiFeO3 to investigate their ionization energies with respect to the free polaron level in pristine BiFeO₃.

When an oxygen vacancy (V_O) is formed in the lattice of BiFeO₃, it introduces two electrons that spontaneously generate two small electron-polaron states. These two states correspond to the two peaks shown ~ 0.8 eV below the CBM in the PDOS of BiFeO₃ in Figure 7a. As in the case of

introducing a free electron-polaron, these polaron states have mainly the t_{2g} character of Fe²⁺. Due to attractive electrostatic interactions between the electron-polarons and the V_O site, the most thermodynamically stable configuration is that with the two electron-polarons located at the Fe sites nearest to the V_O, as shown in Figure 7b. The difference in energy of the V_O polarons seen in the PDOS is a result of their differing distances from the V_O (Figure S7). Introduction of V_O and the resulting small electron-polarons also generate perturbed valence states above the VBM. These perturbed states are mainly composed of the e_{σ} orbitals (i.e., $d_{x^2-y^2}$) of Fe²⁺ and 2p orbitals of oxygen (Figure S8). When absorption spectra of BiFeO₃ with and without V_O were simulated and compared (Figure S9), we found that the presence of the perturbed states above the VBM did not affect the absorption of BiFeO₃. This agrees with our experimental results.

 V_O as a Shallow Donor in BiFeO₃. In order to consider the effects of oxygen vacancies on the carrier concentration in BiFeO₃, it is necessary to compute the formation energy of the defect in each of its charge states q

$$FE_{q}[\varepsilon_{\mathrm{F}}] = E_{q} - E_{\mathrm{pst}} + \sum_{i} \mu_{i} \Delta N_{i} + q \varepsilon_{\mathrm{F}} + \Delta_{q}$$

Here, FE_q is the formation energy of a defect with charge q, E_q is the total energy of the defect system with charge q, $E_{\rm pst}$ is the total energy of the pristine system, ΔN_i is the change in the number of atomic species i with chemical potential μ_{i} , $\varepsilon_{\rm F}$ is the Fermi energy, and Δ_q is the defect charge correction consistent with recent developments 30,31 that serves to remove spurious interactions of the charged defect with its periodic images and with the uniform compensating background charge. The value of the Fermi level $(\varepsilon_{\rm F})$ in which the system undergoes a transition of charge state q to q' defines the charge transition level $\varepsilon^{q|q'}$

$$\varepsilon^{q|q'} = \frac{FE_q[\varepsilon_F] - FE_{q'}[\varepsilon_F]}{a' - a}$$

Typically, the charge transition level of an electron donor from one charge state to a more positive charge state referenced to the CBM defines the ionization energy of the defect. However, in polaronic oxides, the feasibility of polaron

hopping is determined not by the ionization energy of the defect with respect to the CBM but by the ionization energy of the defect with respect to a free polaron state where the polaron is not bound to a defect. Therefore, the true ionization energy of small polarons is equal to the energy difference between the charge transition levels of the defects (solid red dots in Figure 7c) and the free polaron level (gray dashed line in Figure 7c). The free polaron energy level can be obtained from the formation energy of the pristine system with (q=-1) and without (q=0) an extra electron. The Fermi level corresponding to the ε^{0l-1} transition in the pristine system defines the free polaron level. The energy difference between the free polaron level and the CBM is the polaron binding energy.

Under this model, we computed the charge formation energy diagram of the Vo and its corresponding ionization energies. In an oxygen-rich environment, the formation energy of a neutral V_O is 3.4 eV, which agrees with previous calculations. ^{12,40,48,49} We find that the V_O has two distinct charge transition levels corresponding to the (0/+1) and (+1/-1)+2) transitions. The energies of these charge transition levels relative to the VBM (1.57 and 1.22 eV, respectively) are in excellent agreement with recent DFT+U calculations. 42 On the other hand, the positions of charge transition levels relative to the CBM of BiFeO₃ vary drastically depending on the choice of U, 12,42,48 which is a known effect. However, their positions with respect to the free polaron level are relatively insensitive to the choice of U, which is similar to what was reported for the case of Sn-doped Fe_2O_3 . ¹⁹ Comparing the charge transition levels of V_O to the free polaron level, we found energy differences of 99 and 438 meV for the first and second charge transition levels, respectively. The energy of the first charge transition level (0/+1) relative to the free polaron level is comparable to kT at room temperature (26 meV) and indicates that a fraction of the oxygen vacancies in BiFeO3 can ionize at room temperature and contribute to an increased carrier concentration. A simple thermodynamic calculation (assuming a Boltzmann-like distribution) suggests that ~2.05% of oxygen vacancies will be ionized to their +1 state at room temperature at thermal equilibrium. This result differs from previous reports that V_0 in BiFeO₃ is a deep donor and cannot increase the carrier concentration 12,40,48,49 increase the carrier concentration.

Our theoretical result has clarified the role of oxygen vacancies in enhancing carrier concentrations in $BiFeO_3$, and it is consistent with our experimental findings. This study emphasizes that in polaronic oxides, the defect ionization energies need to be considered with respect to the free polaron level and not to the CBM to more accurately understand the role of defects in the charge transport properties.

4. CONCLUSIONS

To summarize, we performed combined experimental and theoretical investigations on n-type $BiFeO_3$ to evaluate its properties relevant to its use as a photoanode in a photoelectrochemical cell. In our experimental study, we developed a synthesis method to produce high-quality, uniform n-type $BiFeO_3$ photoanodes and examined their photoelectrochemical properties. A bandgap energy of ~ 2.1 eV was determined for the $BiFeO_3$ photoanodes, and this value agreed well with the films' orange color. The $BiFeO_3$ photoanode showed a photocurrent onset potential of 0.3 V vs RHE for sulfite oxidation, which is equivalent to its flatband potential. This value is significantly more negative than that of

other ternary Fe-based oxide photoanodes. Upon annealing under a N₂ environment to intentionally introduce more oxygen vacancies, the flatband potential was slightly shifted to the negative direction and the photocurrent increased considerably. These results indicate that oxygen vacancies can contribute to an increase in carrier density, thus improving the charge transport properties of BiFeO₃. While the photocurrent reported in this study is one of the highest among those reported for BiFeO₃ photoanodes, the observed value was still far below that expected for a photoanode having a bandgap of 2.1 eV, suggesting that bulk recombination is a major limitation of BiFeO₃. Considering that nanostructuring other Fe³⁺-containing photoanodes such as Fe₂O₃ that suffer from short hole-diffusion lengths can significantly increase electron-hole separation, nanostructuring BiFeO3 is a logical next step to take to improve its photocurrent generation.

In our theoretical study, we showed for the first time that an extra electron in BiFeO $_3$ spontaneously localizes on an Fe $^{3+}$ ion and forms a small polaron. Formation of the small polaron also perturbs valence states and creates additional localized states above the VBM of pristine BiFeO $_3$. When an oxygen vacancy is introduced into the BiFeO $_3$ lattice, it forms two electron–polarons at the two Fe sites nearest to the V $_0$ site. By accurately referencing the charge transition level to the free electron–polaron level instead of to the CBM in our charge formation energy calculations, we showed that the first ionization energy of V $_0$ is 99 meV, meaning that V $_0$ is capable of serving as a donor to enhance the carrier concentration of BiFeO $_3$.

Overall, BiFeO₃ has many attractive properties for use as a photoanode in a water-splitting PEC, and we expect that strategies such as nanostructuring and substitutional doping that can introduce shallow donors can continue to increase the photocurrent generation. Our combined investigation contributes to a fundamental understanding of the photoelectrochemical properties of BiFeO₃ that can aid future systematic investigations of both n-type and p-type BiFeO₃ photoelectrodes.

ASSOCIATED CONTENT

Supporting Information

The Supporting Information is available free of charge at https://pubs.acs.org/doi/10.1021/acs.chemmater.0c00545.

SEM images, absorption spectra, XRD patterns, photocurrent measurements, XPS spectra, additional band structures, PDOS, and wave function results (PDF)

AUTHOR INFORMATION

Corresponding Authors

Kyoung-Shin Choi — Department of Chemistry, University of Wisconsin, Madison, Wisconsin 53706, United States; orcid.org/0000-0003-1945-8794; Email: kschoi@chem.wisc.edu

Yuan Ping — Department of Chemistry and Biochemistry, University of California, Santa Cruz, California 95064, United States; ⊚ orcid.org/0000-0002-0123-3389; Email: yuanping@ucsc.edu

Authors

Andjela Radmilovic – Department of Chemistry, University of Wisconsin, Madison, Wisconsin 53706, United States

Tyler J. Smart — Department of Physics, University of California, Santa Cruz, California 95064, United States

Complete contact information is available at: https://pubs.acs.org/10.1021/acs.chemmater.0c00545

Author Contributions

§A.R. and T.J.S.: These authors contributed equally. **Notes**

The authors declare no competing financial interest.

ACKNOWLEDGMENTS

K.-S.C. acknowledges financial support by the Division of Chemical Sciences, Geosciences, and Biosciences, Office of Basic Energy Sciences of the U.S. Department of Energy through Grant DE-SC0008707. Y.P. acknowledges financial support from the National Science Foundation under Grants DMR-1760260 and CHE-1904547. Y.P. used resources of the Center for Functional Nanomaterials, which is a U.S. DOE Office of Science Facility, and the Scientific Data and Computing Center, a component of the Computational Science Initiative, at Brookhaven National Laboratory under Contract No. DE-SC0012704. Y.P. also used the lux supercomputer at UC Santa Cruz, funded by NSF MRI Grant AST-1828315, and the Extreme Science and Engineering Discovery Environment (XSEDE), which is supported by National Science Foundation grant number ACI1548562.

REFERENCES

- (1) Choi, T.; Lee, S.; Choi, Y. J.; Kiryukhin, V.; Cheong, S. W. Switchable Ferroelectric Diode and Photovoltaic Effect in BiFeO₃. *Science* **2009**, 324, 63–66.
- (2) Yi, H. T.; Choi, T.; Choi, S. G.; Oh, Y. S.; Cheong, S. W. Mechanism of the Switchable Photovoltaic Effect in Ferroelectric BiFeO₃. *Adv. Mater.* **2011**, *23*, 3403–3407.
- (3) You, L.; Zheng, F.; Fang, L.; Zhou, Y.; Tan, L. Z.; Zhang, Z. Y.; Ma, G. H.; Schmidt, D.; Rusydi, A.; Wang, L.; Chang, L.; Rappe, A. M.; Wang, J. L. Enhancing Ferroelectric Photovoltaic Effect by Polar Order Engineering. *Sci. Adv.* **2018**, *4*, No. eaat3438.
- (4) Spanier, J. E.; Fridkin, V. M.; Rappe, A. M.; Akbashev, A. R.; Polemi, A.; Qi, Y. B.; Gu, Z. Q.; Young, S. M.; Hawley, C. J.; Imbrenda, D.; Xiao, G.; Bennett-Jackson, A. L.; Johnson, C. L. Power Conversion Efficiency Exceeding the Shockley-Queisser Limit in a Ferroelectric Insulator. *Nat. Photonics* **2016**, *10*, 611–616.
- (5) Shen, H.; Zhou, X.; Dong, W.; Su, X.; Fang, L.; Wu, X.; Shen, M. Dual Role of TiO₂ Buffer Layer in Pt Catalyzed BiFeO₃ Photocathodes: Efficiency Enhancement and Surface Protection. *Appl. Phys. Lett.* **2017**, *111*, 123901.
- (6) Yilmaz, P.; Yeo, D.; Chang, H.; Loh, L.; Dunn, S. Perovskite BiFeO₃ Thin Film Photocathode Performance with Visible Light Activity. *Nanotechnology* **2016**, *27*, 345402.
- (7) Moniz, S. J. A.; Blackman, C. S.; Southern, P.; Weaver, P. M.; Tang, J.; Carmalt, C. J. Visible-Light Driven Water Splitting over BiFeO₃ Photoanodes Grown via the LPCVD Reaction of [Bi(O^tBu)₃] and [Fe(O^tBu)₃]₂ and Enhanced with a Surface Nickel Oxygen Evolution Catalyst. *Nanoscale* **2015**, *7*, 16343–16353.
- (8) Song, J.; Kim, T. L.; Lee, J.; Cho, S. Y.; Cha, J.; Jeong, S. Y.; An, H.; Kim, W. S.; Jung, Y.-S.; Park, J.; et al. Domain-Engineered BiFeO₃ Thin-Film Photoanodes for Highly Enhanced Ferroelectric Solar Water Splitting. *Nano Res.* **2018**, *11*, 642–655.
- (9) Liu, Q.; Zhou, Y.; You, L.; Wang, J.; Shen, M.; Fang, L. Enhanced Ferroelectric Photoelectrochemical Properties of Polycrystalline BiFeO₃ Film by Decorating with Ag Nanoparticles. *Appl. Phys. Lett.* **2016**, *108*, 022902.
- (10) Sivula, K.; van de Krol, R. Semiconducting Materials for Photoelectrochemical Energy Conversion. *Nat. Rev.* **2016**, *1*, 1–16.

- (11) Lee, D. K.; Lee, D.; Lumley, M. A.; Choi, K.-S. Progress on Ternary Oxide-Based Photoanodes for Use in Photoelectrochemical Cells for Solar Water Splitting. *Chem. Soc. Rev.* **2019**, *48*, 2126–2157.
- (12) Paudel, T. R.; Jaswal, S. S.; Tsymbal, E. Y. Intrinsic Defects in Multiferroic BiFeO₃ and Their Effect on Magnetism. *Phys. Rev. B: Condens. Matter Mater. Phys.* **2012**, *85*, 104409.
- (13) Rojac, T.; Bencan, A.; Drazic, G.; Sakamoto, N.; Ursic, H.; Jancar, B.; Tavcar, G.; Makarovic, M.; Walker, J.; Malic, B.; Damjanovic, D. Domain-Wall Conduction in Ferroelectric BiFeO₃ Controlled by Accumulation of Charged Defects. *Nat. Mater.* **2017**, *16*, 322–327.
- (14) Cao, D.; Wang, Z.; Nasori; Wen, L.; Mi, Y.; Lei, Y. Switchable Charge-Transfer in the Photoelectrochemical Energy-Conversion Process of Ferroelectric BiFeO₃ Photoelectrodes. *Angew. Chem., Int. Ed.* **2014**, *53*, 11027–11031.
- (15) Huang, Y.-L.; Chang, W. S.; Van, C. N.; Liu, H.-J.; Tsai, K.-A.; Chen, J.-W.; Kuo, H.-H.; Tzeng, W.-Y.; Chen, Y.-C.; Wu, C.-L.; Luo, C.-W.; Hsu, Y.-J.; Chu, Y.-H. Tunable Photoelectrochemical Performance of Au/BiFeO₃ Heterostructure. *Nanoscale* **2016**, *8*, 15795–15801.
- (16) Wheeler, G. P.; Baltazar, V. U.; Smart, T. J.; Radmilovic, A.; Ping, Y.; Choi, K. S. Combined Theoretical and Experimental Investigations of Atomic Doping to Enhance Photon Absorption and Carrier Transport of LaFeO₃ Photocathodes. *Chem. Mater.* **2019**, *31*, 5890–5899.
- (17) Smart, T. J.; Pham, T. A.; Ping, Y.; Ogitsu, T. Optical Absorption Induced by Small Polaron Formation in Transition Metal Oxides: The Case of Co₃O₄. *Phys. Rev. Mater.* **2019**, *3*, 102401.
- (18) Smart, T. J.; Cardiel, A. C.; Wu, F.; Choi, K. S.; Ping, Y. Mechanistic Insights of Enhanced Spin Polaron Conduction in CuO through Atomic Doping. *npj Comput. Mater.* **2018**, *4*, 61.
- (19) Smart, T. J.; Ping, Y. Effect of Defects on the Small Polaron Formation and Transport Properties of Hematite from First-Principles Calculations. *J. Phys.: Condens. Matter* **2017**, *29*, 394006.
- (20) Seo, H.; Ping, Y.; Galli, G. Role of Point Defects in Enhancing the Conductivity of BiVO₄. *Chem. Mater.* **2018**, *30*, 7793–7802.
- (21) Kim, T. W.; Ping, Y.; Galli, G. A.; Choi, K.-S. Simultaneous Enhancements in Photon Absorption and Charge Transport of Bismuth Vanadate Photoanodes for Solar Water Splitting. *Nat. Commun.* **2015**, *6*, 8769.
- (22) Kan, D.; Anbusathaiah, V.; Takeuchi, I. Chemical Substitution-Induced Ferroelectric Polarization Rotation in BiFeO₃. *Adv. Mater.* **2011**, 23, 1765–1769.
- (23) Neaton, J. B.; Ederer, C.; Waghmare, U. V.; Spaldin, N. A.; Rabe, K. M. First-Principles Study of Spontaneous Polarization in Multiferroic BiFeO₃. *Phys. Rev. B: Condens. Matter Mater. Phys.* **2005**, 71, 014113.
- (24) Young, S. M.; Zheng, F.; Rappe, A. M. First-Principles Calculation of the Bulk Photovoltaic Effect in Bismuth Ferrite. *Phys. Rev. Lett.* **2012**, *109*, 236601.
- (25) Liu, S.; Grinberg, I.; Rappe, A. M. Development of a Bond-Valence Based Interatomic Potential for BiFeO₃ for Accurate Molecular Dynamics Simulations. *J. Phys.: Condens. Matter* **2013**, 25, 102202.
- (26) Wang, D. W.; Weerasinghe, J.; Bellaiche, L. Atomistic Molecular Dynamic Simulations of Multiferroics. *Phys. Rev. Lett.* **2012**, *109*, 067203.
- (27) Chang, C. M.; Mani, B. K.; Lisenkov, S.; Ponomareva, I. Prediction of Electromagnons in Antiferromagnetic Ferroelectrics from First-Principles: The Case of BiFeO₃. Ferroelectrics **2016**, 494, 68–75.
- (28) Giannozzi, P.; Baroni, S.; Bonini, N.; Calandra, M.; Car, R.; Cavazzoni, C.; Ceresoli, D.; Chiarotti, G. L.; Cococcioni, M.; Dabo, I.; Dal Corso, A.; de Gironcoli, S.; Fabris, S.; Fratesi, G.; Gebauer, R.; Gerstmann, U.; Gougoussis, C.; Kokalj, A.; Lazzeri, M.; Martin-Samos, L.; Marzari, N.; Mauri, F.; Mazzarello, R.; Paolini, S.; Pasquarello, A.; Paulatto, L.; Sbraccia, C.; Scandolo, S.; Sclauzero, G.; Seitsonen, A. P.; Smogunov, A.; Umari, P.; Wentzcovitch, R. M. QUANTUM ESPRESSO: A Modular and Open-Source Software

- Project For Quantum Simulations of Materials. J. Phys.: Condens. Matter 2009, 21, 395502.
- (29) Garrity, K. F.; Bennett, J. W.; Rabe, K. M.; Vanderbilt, D. Pseudopotentials for High-Throughput DFT Calculations. *Comput. Mater. Sci.* **2014**, *81*, 446–452.
- (30) Sundararaman, R.; Ping, Y. First-Principles Electrostatic Potentials for Reliable Alignment at Interfaces and Defects. *J. Chem. Phys.* **2017**, *146*, 104109.
- (31) Sundararaman, R.; Letchworth-Weaver, K.; Schwarz, K. A.; Gunceler, D.; Ozhabes, Y.; Arias, T. A. JDFTx: Software for Joint Density-Functional Theory. *SoftwareX* 2017, 6, 278–284.
- (32) Marini, A.; Hogan, C.; Gruning, M.; Varsano, D. yambo: An Ab Initio Tool for Excited State Calculations. *Comput. Phys. Commun.* **2009**, *180*, 1392–1403.
- (33) Jackson, J. D. Classical Electrodynamics; John Wiley & Sons, Inc.: New York, 1999.
- (34) Cucka, P.; Barrett, C. S. The Crystal Structure of Bi and of Solid Solutions of Pb, Sn, Sb and Te in Bi. *Acta Crystallogr.* **1962**, *15*, 865–872.
- (35) Govindaraju, G. V.; Wheeler, G. P.; Lee, D.; Choi, K.-S. Methods for Electrochemical Synthesis and Photoelectrochemical Characterization for Photoelectrodes. *Chem. Mater.* **2017**, *29*, 355–370.
- (36) Jang, J.-W.; Friedrich, D.; Müller, S.; Lamers, M.; Hempel, H.; Lardhi, S.; Cao, Z.; Harb, M.; Cavallo, L.; Heller, R.; Eichberger, R.; van de Krol, R.; Abdi, F. F. Enhancing Charge Carrier Lifetime in Metal Oxide Photoelectrodes through Mild Hydrogen Treatment. *Adv. Energy Mater.* **2017**, *7*, 1701536.
- (37) Cooper, J. K.; Scott, S. B.; Ling, Y.; Yang, J.; Hao, S.; Li, Y.; Toma, F. M.; Stutzmann, M.; Lakshmi, K. V.; Sharp, I. D. Role of Hydrogen in Defining the n-Type Character of BiVO₄ Photoanodes. *Chem. Mater.* **2016**, 28, 5761–5771.
- (38) Liu, D.; Liu, Y.; Garcia, B. B.; Zhang, Q.; Pan, A.; Jeong, Y.-H.; Cao, G. V_2O_5 Xerogel Electrodes with Much Enhanced Lithium-Ion Intercalation Properties with N_2 Annealing. *J. Mater. Chem.* **2009**, *19*, 8789–8795.
- (39) Redfern, S. A. T.; Wang, C.; Hong, J. W.; Catalan, G.; Scott, J. F. Elastic and Electrical Anomalies at Low-Temperature Phase Transitions in BiFeO₃. *J. Phys.: Condens. Matter* **2008**, *20*, 452205.
- (40) Kay, A.; Cesar, I.; Grätzel, M. New Benchmark for Water Photooxidation by Nanostructured α -Fe₂O₃ Films. *J. Am. Chem. Soc.* **2006**, *128*, 15714–15721.
- (41) Guo, Y.; Fu, Y.; Liu, Y.; Shen, S. Photoelectrochemical Activity of ZnFe_2O_4 Modified $\alpha\text{-Fe}_2\text{O}_3$ Nanorod Array Films. *RSC Adv.* **2014**, 4, 36967–36972.
- (42) Geneste, G.; Paillard, C.; Dkhil, B. Polarons, Vacancies, Vacancy Associations, and Defect States in Multiferroic BiFeO₃. *Phys. Rev. B: Condens. Matter Mater. Phys.* **2019**, 99, 024104.
- (43) Lu, J.; Gunther, A.; Schrettle, F.; Mayr, F.; Krohns, S.; Lunkenheimer, P.; Pimenov, A.; Travkin, V. D.; Mukhin, A. A.; Loidl, A. On the Room Temperature Multiferroic BiFeO₃: Magnetic, Dielectric and Thermal Properties. *Eur. Phys. J. B* **2010**, 75, 451–460.
- (44) Gheorghiu, F.; Calugaru, M.; Ianculescu, A.; Musteata, V.; Mitoseriu, L. Preparation and Functional Characterization of BiFeO₃ Ceramics: A Comparative Study of the Dielectric properties. *Solid State Sci.* **2013**, 23, 79–87.
- (45) Wu, F.; Ping, Y. Combining Landau-Zener Theory and Kinetic Monte Carlo Sampling for Small Polaron Mobility of Doped BiVO₄ from First-Principles. *J. Mater. Chem. A* **2018**, *6*, 20025–20036.
- (46) Zhang, W. R.; Wu, F.; Li, J.; Yan, D. H.; Tao, J.; Ping, Y.; Liu, M. Z. Unconventional Relation between Charge Transport and Photocurrent via Boosting Small Polaron Hopping for Photoelectrochemical Water Splitting. ACS Energy Lett. 2018, 3, 2232–2239.
- (47) Baettig, P.; Ederer, C.; Spaldin, N. A. First Principles Study of the Multiferroics BiFeO₃, Bi₂FeCrO₆, and BiCrO₃: Structure, Polarization, and Magnetic Ordering Temperature. *Phys. Rev. B: Condens. Matter Mater. Phys.* **2005**, 72, 214105.

- (48) Zhang, Z.; Wu, P.; Chen, L.; Wang, J. L. Density Functional Theory Plus U Study of Vacancy Formations in Bismuth Ferrite. *Appl. Phys. Lett.* **2010**, *96*, 232906.
- (49) Shimada, T.; Matsui, T.; Xu, T.; Arisue, K.; Zhang, Y. J.; Wang, J.; Kitamura, T. Multiferroic Nature of Intrinsic Point Defects in BiFeO₃: A Hybrid Hartree-Fock Density Functional Study. *Phys. Rev. B: Condens. Matter Mater. Phys.* **2016**, *93*, 174107.